

# Deeply virtual Compton scattering in the tensor-pomeron approach

Piotr Lebiedowicz,<sup>1,\*</sup> Otto Nachtmann,<sup>2,†</sup> and Antoni Szczurek<sup>c1,§</sup>

<sup>1</sup>*Institute of Nuclear Physics Polish Academy of Sciences,  
Radzikowskiego 152, PL-31342 Kraków, Poland*

<sup>2</sup>*Institut für Theoretische Physik, Universität Heidelberg,  
Philosophenweg 16, D-69120 Heidelberg, Germany*

## Abstract

The two-tensor-pomeron model proposed previously to describe low  $x$  DIS data is applied to real and virtual Compton scattering on a proton. The model includes two tensor pomerons, a soft and a hard one, and tensor reggeons. We include contributions of both transverse and longitudinal virtual photons. We show that this model gives a very good description of experimental data at small Bjorken  $x$  on deeply virtual Compton scattering (DVCS) from HERA. The reggeon exchange term is particularly relevant for describing the real-photon-proton scattering measured at lower  $\gamma p$  energies at FNAL. We present two fits which differ somewhat in the strength of the hard pomeron contribution. In both fits we find that the interference between soft- and hard-pomeron exchange plays an important role. We find that in DVCS the soft-pomeron contribution is considerable up to  $Q^2 \sim 20 \text{ GeV}^2$ . Our model allows to study the transition from the small- $Q^2$  regime, including the photoproduction ( $Q^2 = 0$ ) limit, to the large- $Q^2$  regime, the DIS limit. We also discuss the ratio of cross sections for longitudinally and transversely polarized virtual photons in  $\gamma^* p \rightarrow \gamma p$  as a function of  $|t|$  and  $Q^2$ . The ratio  $\tilde{R}(Q^2, W^2, t) = (d\sigma_L/dt)/(d\sigma_T/dt)$  strongly increases with  $t$ . Our findings may be checked in future lepton-nucleon scattering experiments in the low- $x$  regime, for instance, at a future Electron-Ion Collider at the BNL (EIC), and, if LHeC is realized, at the LHC.

---

<sup>c</sup> Also at College of Natural Sciences, Institute of Physics, University of Rzeszów, ul. Pigonia 1, PL-35310 Rzeszów, Poland.

<sup>\*</sup> Piotr.Lebiedowicz@ifj.edu.pl

<sup>†</sup> O.Nachtmann@thphys.uni-heidelberg.de

<sup>§</sup> Antoni.Szczurek@ifj.edu.pl

## I. INTRODUCTION

In this Letter we apply the two-tensor-pomeron model [1] to deeply virtual Compton scattering (DVCS) on the proton ( $\gamma^* p \rightarrow \gamma p$ ). This Regge type model can be used for large  $\gamma^* p$  centre-of-mass energy  $W \gg m_p$ ,  $\sqrt{|t|}$ ,  $|t| \lesssim 1 \text{ GeV}^2$ , and small Bjorken- $x$ , say  $x = Q^2/(W^2 + Q^2 - m_p^2) < 0.02$ . Here  $m_p$  is the proton mass,  $Q^2$  is the photon virtuality, and  $t$  is the squared momentum transfer at the proton vertex.

The DVCS has been a subject of extensive experimental and theoretical research; see e.g. [2–11] for theory papers. For a review and many references see [5]. Recently, the possibility of probing the nonlinear (saturation) effects on the DVCS process was considered in [12–14]. A comprehensive experimental overview of DVCS is presented in [15]; see also Fig. 5 of [16] which shows the kinematic coverage in the  $x$ - $Q^2$  plane for existing DVCS measurements, as well as planned ones. The H1 [17, 18] and ZEUS [19, 20] Collaborations measured the DVCS cross section over a broad range of  $W$  and  $Q^2$  at low Bjorken- $x$ . Also the differential cross section  $d\sigma/dt$  was extracted. In [18] the beam charge asymmetry due to the interference between the DVCS and the purely electromagnetic Bethe-Heitler process was measured. The HERMES Collaboration [21–23] performed measurements of single- and double-spin DVCS asymmetries. The Jefferson Lab CLAS Collaboration measured DVCS beam-spin asymmetries and cross sections [24–27] and longitudinally polarized target-spin asymmetries [28–30]. The COMPASS Collaboration [31] measured the DVCS cross section by studying exclusive single-photon production in muon-proton scattering,  $\mu p \rightarrow \mu p \gamma$ . The Jefferson Lab Hall A Collaboration measured the photon electroproduction cross section in the valence quark region [32, 33], as well as the DVCS off the neutron [34], and recently [35] the DVCS off the proton at high values of Bjorken- $x$ . Experimental programs at Jefferson Lab, at the Electron Ion Collider (EIC) under construction at BNL [16, 36–38], and, if realized, at a Large Hadron Electron Collider (LHeC) at the LHC [39, 40], are expected to improve our knowledge of DVCS in a wide kinematic range.

DVCS is a prime playground for the application of the generalized parton-distribution (GPD) concept based on perturbative QCD (pQCD), cf. [5] for a review. However, for small values of Bjorken  $x$  the application of pQCD concepts faces the problem that the effective expansion parameter is there  $\alpha_s \ln(1/x)$  which is large for small  $x$ . More phenomenological models are then frequently used, based e.g. on the colour-dipole approach or the Regge approach. In our present work we use the latter approach where the scattering is described using exchange objects. For high energies  $W$  the pomeron will be the most important exchange object. For general reviews of pomeron physics see, e.g., [41–43]. Applications of Regge theory to DVCS have been given in [44, 45] and we shall comment on these papers below.

In the following we shall use the tensor-pomeron model as introduced for soft high-energy reactions in [46] and extended to hard reactions in [1]. The soft and hard pomeron and the charge-conjugation  $C = +1$  reggeons ( $\mathbb{R}_+ = f_{2\mathbb{R}}, a_{2\mathbb{R}}$ ) are described as effective rank-2 symmetric tensor exchanges, the odderon and the  $C = -1$  reggeons ( $\mathbb{R}_- = \rho_{\mathbb{R}}, \omega_{\mathbb{R}}$ ) are described as effective vector exchanges. Applications of this tensor-pomeron concept were given for photoproduction of pion pairs in [47], for a number of exclusive central-production reactions, see for instance [48–53], and for soft-photon radiation (bremsstrahlung) in hadronic collisions [54, 55]. For some remarks on the history of tensor-pomeron concepts and corresponding references see [56].

Now we wish to discuss some arguments why we think that soft and hard pomeron should be described as effective tensor objects. It was shown in [1] that considering these pomerons as vector objects leads to the conclusion that they decouple in the total photoabsorption cross section on the proton and in the structure functions of low- $x$  deep inelastic scattering (DIS). But experiment clearly shows pomeron-exchange behaviour for these quantities at large  $W$ . A scalar nature of the pomeron could be excluded in [56] through a comparison of spin-dependent proton-proton elastic scattering with theory. The ratio of single-flip to non-flip amplitudes as measured in [57] is in complete disagreement with the prediction from the scalar pomeron but agrees nicely with that from the tensor pomeron; see [56]. A tensor nature of the soft pomeron is also preferred in holographic-QCD approaches; see e.g. [58, 59]. A two-pomeron description of low- $x$  DIS was first proposed in [60]. However, there a vector nature of the pomerons was considered and this, at closer look, leads to the conclusion of their decoupling in DIS; see above.

In [1] the two-tensor-pomeron approach was applied to describe simultaneously the experimental data on the inclusive cross sections for DIS at low  $x$  [61] and for photoproduction. The global fit performed there was based on the hard and soft pomeron, and the reggeon  $f_{2\mathbb{R}} + a_{2\mathbb{R}}$ . The model describes the transition from the low- $Q^2$  regime, including the  $Q^2 = 0$  photoproduction limit, where the real or virtual photon behaves hadronlike and the soft pomeron dominates, to the large- $Q^2$  regime which is the domain of the hard pomeron. For the photoproduction cross section  $\sigma_{\gamma p}(W)$  no significant contribution from the hard pomeron was found. In this model  $\sigma_{\gamma p}(W)$  is, in the range  $6 \text{ GeV} < W < 209 \text{ GeV}$ , dominated by soft-pomeron exchange with a significant reggeon contribution for  $W < 30 \text{ GeV}$ . The transition region where both pomerons contribute significantly was found to be roughly  $0 < Q^2 < 20 \text{ GeV}^2$ . But as  $Q^2$  increases the hard-pomeron component becomes more and more important.

The Letter is organized as follows. In the next section we introduce the tensor-pomeron approach for real and deeply virtual Compton scattering on a proton. Section III presents the comparison of our model results with experimental data. There we also discuss theoretical uncertainties and limitations of the model. Section IV contains our conclusions.

## II. THEORETICAL FORMALISM

We investigate the real and deeply virtual Compton scattering on a proton

$$\gamma^{(*)}(q, \epsilon) + p(p, \lambda) \rightarrow \gamma(q', \epsilon') + p(p', \lambda'). \quad (2.1)$$

The momenta are indicated in brackets,  $\lambda, \lambda' \in \{1/2, -1/2\}$  are the proton helicities, and  $\epsilon, \epsilon'$  are the photon polarization vectors.

For an initial virtual photon  $\gamma^*$  the reaction (2.1) is extracted from  $ep \rightarrow ep\gamma$  scattering (see Fig. 1)

$$e(k) + p(p, \lambda) \rightarrow e(k') + \gamma(q', \epsilon') + p(p', \lambda'). \quad (2.2)$$

Here the Bethe-Heitler process and DVCS contribute with the latter corresponding to electroproduction of the  $\gamma p$  state. A detailed kinematic analysis of electroproduction reactions can e.g. be found in [62] where, in particular, many relations of variables in the rest system of the original proton and in the system used in HERA experiments are given.

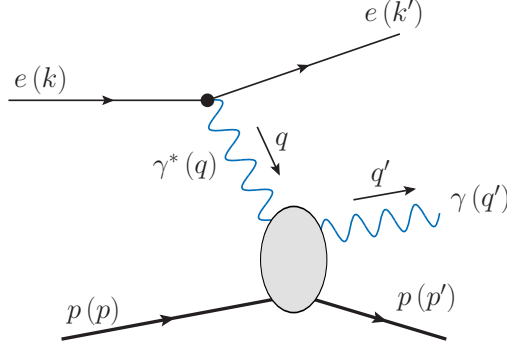


FIG. 1. DVCS contribution to  $ep \rightarrow ep\gamma$  (2.2).

The standard kinematic variables for (2.1) and (2.2), setting the electron mass to zero, are (see Table 1 of [62])

$$\begin{aligned}
q &= k - k', \quad q^2 = -Q^2, \\
s &= (p + k)^2, \\
t &= (p - p')^2, \quad t \leq -|t|_{\min}, \\
W^2 &= (p + q)^2, \\
x &= \frac{Q^2}{2p \cdot q} = \frac{Q^2}{W^2 + Q^2 - m_p^2}, \\
y &= \frac{p \cdot q}{p \cdot k} = \frac{W^2 + Q^2 - m_p^2}{s - m_p^2}, \\
\varepsilon &= \frac{2(1 - y) - 2xym_p^2(s - m_p^2)^{-1}}{1 + (1 - y)^2 + 2xym_p^2(s - m_p^2)^{-1}}.
\end{aligned} \tag{2.3}$$

Here  $\varepsilon$  is the ratio of longitudinal and transverse polarization strengths of the virtual photon  $\gamma^*$  and  $t = -|t|_{\min}$  corresponds to forward scattering. For  $Q^2 = 0$  we have  $|t|_{\min} = 0$  and for  $W^2 \gg Q^2, m_p^2$  we find (see also Appendix A of [62])

$$|t|_{\min} = Q^2 \left[ \frac{Q^2 m_p^2}{W^4} + \mathcal{O} \left( \frac{Q^6}{W^6}, \frac{Q^4 m_p^2}{W^6}, \frac{Q^2 m_p^4}{W^6}, \frac{m_p^6}{W^6} \right) \right]. \tag{2.4}$$

We assume for (2.2) unpolarized initial particles and no observation of the polarization of final state particles.

Adapting (3.20) and (3.21) of [62] to the reaction (2.2) and integrating over the azimuthal angle  $\varphi$  defined in (2.1) of [62] we get for the DVCS part of (2.2)

$$\frac{d\sigma(ep \rightarrow ep\gamma)}{dydQ^2dt} = \Gamma_{ep\gamma} \left( \frac{d\sigma_T}{dt}(Q^2, W^2, t) + \varepsilon \frac{d\sigma_L}{dt}(Q^2, W^2, t) \right). \tag{2.5}$$

Here, with Hand's convention [63], the  $\gamma^*$  flux factor reads

$$\Gamma_{ep\gamma} = \frac{\alpha_{\text{em}}}{\pi y Q^2} \left( 1 - y + \frac{1}{2} y^2 + xy \frac{m_p^2}{s - m_p^2} \right) \frac{W^2 - m_p^2}{W^2 - m_p^2 + Q^2 + 4xm_p^2}, \tag{2.6}$$

where  $\alpha_{\text{em}}$  is the fine structure constant. Furthermore,  $d\sigma_{\text{T}}/dt$  and  $d\sigma_{\text{L}}/dt$  are the differential cross sections for  $\gamma^* p \rightarrow \gamma p$  for transverse and longitudinal polarization of the  $\gamma^*$ ,

$$\begin{aligned}\frac{d\sigma_{\text{T}}}{dt}(Q^2, W^2, t) &= \frac{1}{2} \left( \frac{d\sigma_{++}}{dt}(Q^2, W^2, t) + \frac{d\sigma_{--}}{dt}(Q^2, W^2, t) \right), \\ \frac{d\sigma_{\text{L}}}{dt}(Q^2, W^2, t) &= \frac{d\sigma_{00}}{dt}(Q^2, W^2, t),\end{aligned}\quad (2.7)$$

where

$$\begin{aligned}\frac{d\sigma_{mm}}{dt}(Q^2, W^2, t) &= \frac{1}{16\pi(W^2 - m_p^2)\sqrt{(W^2 - m_p^2 + Q^2)^2 + 4m_p^2 Q^2}} \\ &\times \frac{1}{2} \sum_{\lambda, \lambda', a} \left| \left\langle \gamma(q', \epsilon'_a), p(p', \lambda'), \text{out} \left| eJ_\mu(0) \epsilon_m^\mu \right| p(p, \lambda) \right\rangle \right|^2.\end{aligned}\quad (2.8)$$

Here  $eJ_\mu$  is the electromagnetic current,  $\epsilon_m(m = \pm, 0)$  are the standard  $\gamma^*$  polarization vectors for right and left circular and longitudinal polarization [see (3.11)–(3.14) of [62]] and  $\epsilon'_a(a = 1, 2)$  are the polarization vectors of the real photon in the final state.

So far, everything is completely general. Now we consider the small  $x$  region of DVCS:

$$W \geq m_p, \sqrt{|t|}, \quad |t| \lesssim 1 \text{ GeV}^2, \quad x \leq 0.02. \quad (2.9)$$

There we describe the amplitude for (2.1) in terms of the exchanges of soft ( $\mathbb{P}_1$ ) and hard ( $\mathbb{P}_0$ ) pomeron and the reggeons  $f_{2\mathbb{R}}$  and  $a_{2\mathbb{R}}$ . Only  $C = +1$  exchanges can contribute in (2.1). The properties of  $\mathbb{P}_0, \mathbb{P}_1, f_{2\mathbb{R}}$ , and  $a_{2\mathbb{R}}$ , and their couplings to protons and photons will be taken as in [1]. In this way we get

$$\begin{aligned}\langle \gamma(q', \epsilon'), p(p', \lambda'), \text{out} | eJ_\nu(0) \epsilon^\nu | p(p, \lambda) \rangle &\equiv (\epsilon'^\mu)^* \mathcal{M}_{\mu\nu, \lambda' \lambda} \epsilon^\nu \\ &= -(\epsilon'^\mu)^* \sum_{j=0,1} \Gamma_{\mu\nu\kappa\rho}^{(\mathbb{P}_j \gamma^* \gamma^*)}(q', q) \epsilon^\nu \Delta^{(\mathbb{P}_j) \kappa\rho, \alpha\beta}(W^2, t) \bar{u}_{\lambda'}(p') \Gamma_{\alpha\beta}^{(\mathbb{P}_j pp)}(p', p) u_\lambda(p) \\ &\quad + (\mathbb{P}_j \rightarrow f_{2\mathbb{R}}, a_{2\mathbb{R}}).\end{aligned}\quad (2.10)$$

Here  $\Delta^{(\mathbb{P}_j)}$  and  $\Gamma^{(\mathbb{P}_j pp)}$  denote the effective propagator and proton vertex function, respectively, for the tensor pomeron  $\mathbb{P}_j$ . The corresponding expressions, as given in Appendix A of [1], are as follows

$$i\Delta_{\mu\nu, \kappa\lambda}^{(\mathbb{P}_j)}(W^2, t) = \frac{1}{4W^2} \left( g_{\mu\kappa} g_{\nu\lambda} + g_{\mu\lambda} g_{\nu\kappa} - \frac{1}{2} g_{\mu\nu} g_{\kappa\lambda} \right) (-iW^2 \tilde{\alpha}'_j)^{\alpha_j(t)-1}, \quad (2.11)$$

$$i\Gamma_{\mu\nu}^{(\mathbb{P}_j pp)}(p', p) = -i3\beta_{jpp} F_1^{(j)}(t) \left\{ \frac{1}{2} \left[ \gamma_\mu(p' + p)_\nu + \gamma_\nu(p' + p)_\mu \right] - \frac{1}{4} g_{\mu\nu} (\not{p}' + \not{p}) \right\}. \quad (2.12)$$

The coupling constants  $\beta_{jpp}$  of the pomerons to protons are  $\beta_{0pp} = \beta_{1pp} = 1.87 \text{ GeV}^{-1}$ . The *Ansätze* for effective propagators and vertices for the  $f_{2\mathbb{R}}$  and  $a_{2\mathbb{R}}$  reggeons are analogous to (2.11) and (2.12), respectively. We shall assume identical trajectories for  $f_{2\mathbb{R}}$  and  $a_{2\mathbb{R}}$  and combine their contribution in (2.10) to a reggeon  $\mathbb{R}_+$  term labeled  $j = 2$  as explained in Appendix A of [1]; see (A20)–(A31) of [1].

The pomeron and reggeon trajectory functions are assumed to be of linear form

$$\alpha_j(t) = \alpha_j(0) + \alpha'_j t, \quad \alpha_j(0) = 1 + \epsilon_j, \quad (j = 0, 1, 2). \quad (2.13)$$

In (2.11) the parameters multiplying the squared energy  $W^2$  in the effective propagators are taken as  $\tilde{\alpha}'_j = \alpha'_j$ . The slope parameters  $\alpha'_j$  are taken as the default values from [1]:  $\alpha'_1 = \alpha'_0 = 0.25 \text{ GeV}^{-2}$ ,  $\alpha'_2 = 0.9 \text{ GeV}^{-2}$ . The intercept parameters of the trajectories (2.13) were determined from detailed comparison of the two-tensor-pomeron model with the DIS HERA data and photoproduction data in Ref. [1]:

$$\text{soft pomeron } \mathbb{P}_1 : \quad \epsilon_1 = 0.0935^{(+76}_{-64}), \quad (2.14)$$

$$\text{hard pomeron } \mathbb{P}_0 : \quad \epsilon_0 = 0.3008^{(+73}_{-84}), \quad (2.15)$$

$$\text{reggeon } \mathbb{R}_+ : \quad \alpha_2(0) = 0.485^{(+88}_{-90}). \quad (2.16)$$

Note that for the fit to the DIS structure functions and the total photoabsorption cross section, being related to the absorptive parts of the *forward* virtual and real Compton amplitudes, only the values of the *intercepts* of the pomerons and reggeons enter; see Eqs. (3.7)–(3.10) of [1]. What also enters there are the scale or  $W^2$  parameters  $\tilde{\alpha}'_j$  ( $j = 0, 1, 2$ ). For convenience these were chosen equal to the slope parameters  $\alpha'_j$  ( $j = 0, 1, 2$ ); see (A3), (A7), and (A22) of [1]. But from (3.7)–(3.10) of [1] we see that a change of the  $\tilde{\alpha}'_j$  parameters affects only the values of the coupling parameters and does not affect the values of the intercepts. In (2.14)–(2.16) above we quote the values of  $\epsilon_j = \alpha_j(0) - 1$  for  $j = 0, 1$  and  $\alpha_2(0)$  with errors as they were obtained in [1]. The issue of linearity or non-linearity of the Regge trajectories plays absolutely no role there. In our present work, however, the linearity assumption (2.13) is *important*. For a discussion of the linearity of the trajectories see e.g. the reviews [41, 43]. Non-linear trajectories are discussed, for instance, in [64–72].

The *Ansätze* for the  $\mathbb{P}\gamma^*\gamma^*$  and  $\mathbb{R}_+\gamma^*\gamma^*$  coupling functions for both real and virtual photons are discussed in [1]. The  $\mathbb{P}_j\gamma^*\gamma^*$  vertex, coupling the soft ( $j = 0$ ) and hard ( $j = 1$ ) pomeron to two (virtual or real) photons, reads [see (A18) of [1]]

$$i\Gamma_{\mu\nu\kappa\rho}^{(\mathbb{P}_j\gamma^*\gamma^*)}(q', q) = i \left[ 2a_{j\gamma^*\gamma^*}(q^2, q'^2, t) \Gamma_{\mu\nu\kappa\rho}^{(0)}(q', -q) - b_{j\gamma^*\gamma^*}(q^2, q'^2, t) \Gamma_{\mu\nu\kappa\rho}^{(2)}(q', -q) \right],$$

where  $t = (q - q')^2$ ,  $j = 0, 1$ . (2.17)

The coupling functions  $a_{j\gamma^*\gamma^*}$  and  $b_{j\gamma^*\gamma^*}$  have dimensions  $\text{GeV}^{-3}$  and  $\text{GeV}^{-1}$ , respectively. The rank-4 tensor functions  $\Gamma_{\mu\nu\kappa\rho}^{(i)}$  ( $i = 0, 2$ ) are defined in (A13)–(A17) of [1]. The  $\mathbb{R}_+\gamma^*\gamma^*$  vertex for real and virtual photons has the same structure as (2.17) and is labeled with  $j = 2$ ; see (A27)–(A31) of [1].

Inserting (2.11), (2.12) and (2.17) in (2.10) we get

$$\begin{aligned} \mathcal{M}_{\mu\nu, \lambda'\lambda} = & -i \sum_{j=0,1,2} \left[ 2a_{j\gamma^*\gamma^*}(q^2, 0, t) \Gamma_{\mu\nu\kappa\rho}^{(0)}(q', -q) - b_{j\gamma^*\gamma^*}(q^2, 0, t) \Gamma_{\mu\nu\kappa\rho}^{(2)}(q', -q) \right] \\ & \times \frac{1}{2W^2} (-iW^2 \alpha'_j)^{\alpha_j(t)-1} 3\beta_{jpp} F_1^{(j)}(t) \bar{u}_{\lambda'}(p') \gamma^\kappa(p' + p)^\rho u_\lambda(p). \end{aligned} \quad (2.18)$$

From (2.18) we can read off the parameters of our model. Taking the pomeron and reggeon parameters as specified above for granted  $\mathcal{M}_{\mu\nu,\lambda'\lambda}$  is parametrized by the functions

$$\begin{aligned} & a_{j\gamma^*\gamma^*}(q^2, 0, t) \beta_{jpp} F_1^{(j)}(t), \\ & b_{j\gamma^*\gamma^*}(q^2, 0, t) \beta_{jpp} F_1^{(j)}(t), \\ & j = 0, 1, 2. \end{aligned} \quad (2.19)$$

Here we consider the  $\beta_{jpp}$  as normalization constants with values  $\beta_{0pp} = \beta_{1pp} = 1.87 \text{ GeV}^{-1}$ ,  $\beta_{2pp} = 3.68 \text{ GeV}^{-1}$ , as given in Appendix A of [1].

For forward virtual Compton scattering,  $q^2 = q'^2 = -Q^2$  and  $t = 0$ , we have from (A19), (A30), and (A31) of [1]

$$\begin{aligned} & a_{j\gamma^*\gamma^*}(-Q^2, -Q^2, 0) = e^2 \hat{a}_j(Q^2), \\ & b_{j\gamma^*\gamma^*}(-Q^2, -Q^2, 0) = e^2 \hat{b}_j(Q^2), \\ & j = 0, 1, 2. \end{aligned} \quad (2.20)$$

The coupling functions  $\hat{a}_j(Q^2)$  and  $\hat{b}_j(Q^2)$  were determined from the global fit to HERA inclusive DIS data for  $Q^2 < 50 \text{ GeV}^2$  and  $x < 0.01$  and the ( $Q^2 = 0$ ) photoproduction data; see Appendix C and Table IV of [1].

The  $Q^2$  and  $t$  dependencies of the coupling functions in the  $\mathbb{P}_j\gamma^*\gamma^*$  and  $\mathbb{R}_+\gamma^*\gamma^*$  vertices in (2.18) must be determined from a comparison to experimental data. As we shall show in Sec. III we obtain quite satisfactory descriptions of the DVCS HERA and elastic  $\gamma p$ -scattering FNAL data with the following assumptions:

$$\begin{aligned} & a_{j\gamma^*\gamma^*}(q^2, 0, t) = e^2 \hat{a}_j(Q^2) F^{(j)}(t), \quad (j = 0, 1, 2), \\ & b_{j\gamma^*\gamma^*}(q^2, 0, t) = e^2 \hat{b}_j(Q^2) F^{(j)}(t), \quad (j = 2), \end{aligned} \quad (2.21)$$

and for alternative fits 1 and 2

$$\begin{aligned} \text{FIT 1 : } & b_{1\gamma^*\gamma^*}(q^2, 0, t) = e^2 \hat{b}_1(0) (1 + Q^2/\Lambda_1^2)^{-1.2} F^{(1)}(t), \quad \Lambda_1 = 1.4 \text{ GeV}, \\ & b_{0\gamma^*\gamma^*}(q^2, 0, t) = e^2 \hat{b}_0(Q^2) F^{(0)}(t), \\ \text{FIT 2 : } & b_{1\gamma^*\gamma^*}(q^2, 0, t) = e^2 \hat{b}_1(0) (1 + Q^2/\Lambda_2^2)^{-2.0} F^{(1)}(t), \quad \Lambda_2 = 2.0 \text{ GeV}, \\ & b_{0\gamma^*\gamma^*}(q^2, 0, t) = \begin{cases} e^2 \hat{b}_0(Q^2) F^{(0)}(t) & \text{for } Q^2 < 1.5 \text{ GeV}^2 \\ e^2 \Lambda_0 (1 + Q^2/\Lambda_3^2)^{-0.6} F^{(0)}(t) & \text{for } Q^2 \geq 1.5 \text{ GeV}^2 \end{cases}, \\ & \Lambda_0 = 9.46 \times 10^{-3} \text{ GeV}^{-1}, \quad \Lambda_3 = 2.3 \text{ GeV}. \end{aligned} \quad (2.22)$$

The coupling functions as a function of  $Q^2$  used in the calculations are shown in Fig. 2. Shown are only the middle values of the pomeron- and reggeon- $\gamma^*\gamma^*$  coupling functions up to  $Q^2 = 50 \text{ GeV}^2$  determined from a global fit in [1]. For a detailed discussion of the fit quality see [1]. According to [1], for the  $\mathbb{R}_+$ -reggeon term, the function  $\hat{a}_2(Q^2)$  is assumed to be zero while the function  $\hat{b}_2(Q^2)$  (see the green dotted line) vanishes rapidly with increasing  $Q^2$ . We see that the soft pomeron function  $\hat{b}_1$  is larger than the corresponding hard one  $\hat{b}_0$  up to  $Q^2 \simeq 20 \text{ GeV}^2$ . The function  $\hat{b}_0$  (see the red long-dash-dotted line) is very small for  $Q^2 \rightarrow 0$  and reaches a maximum at  $Q^2 = 1.27 \text{ GeV}^2$  with amplitude  $\hat{b}_0 =$

$0.0082 \text{ GeV}^{-1}$ . This function is important in the large- $Q^2$  region. Thus, it can be expected that the soft pomeron contribution will be essential for understanding the HERA DVCS data. We consider two different parametrizations: (1) FIT 1 (2.22) with the modification of only one pomeron- $\gamma^*\gamma^*$  coupling function  $\hat{b}_1(Q^2)$ , corresponding to a “soft term”; (2) FIT 2 (2.23) with the modification of both  $\hat{b}_1(Q^2)$  and  $\hat{b}_0(Q^2)$ . Here we increase the hard component and decrease the soft one relative to FIT 1. All other coupling functions, in both our fits, are fixed in accord with those from the fit to DIS of [1].

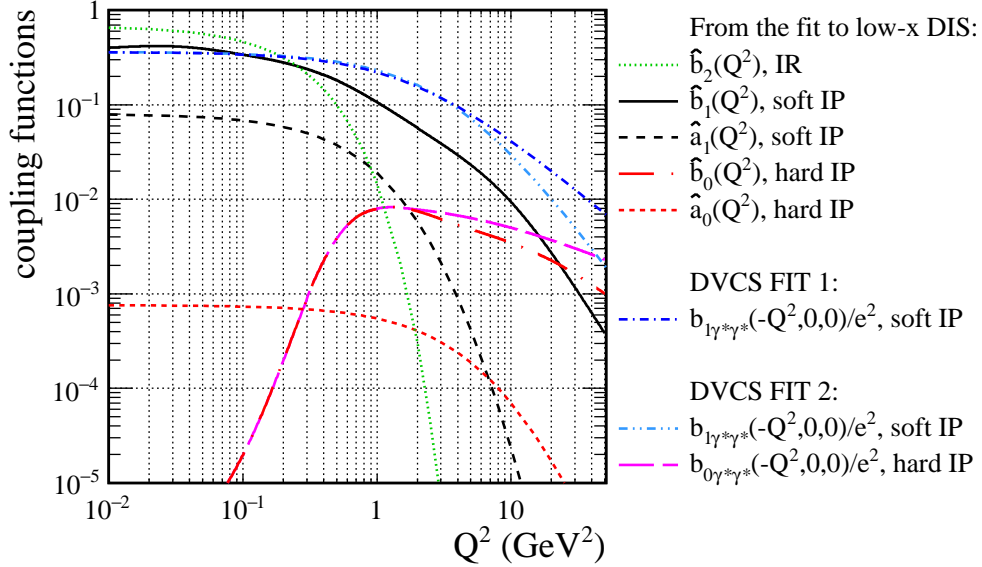


FIG. 2. The pomeron- and reggeon- $\gamma^*\gamma^*$  coupling functions  $\hat{a}_j(Q^2)$  and  $\hat{b}_j(Q^2)$  from (2.20), for  $\mathbb{R}_+$  reggeon ( $j = 2$ , green dotted line), soft pomeron ( $j = 1$ , black solid and dashed lines), and hard pomeron ( $j = 0$ , red long-dash-dotted and short-dashed lines), as determined in [1]. The experimental uncertainties of the fit are not shown here. For this we refer to Figs. 12–15 of [1]. The blue dash-dotted line corresponds to the  $b_{1\gamma^*\gamma^*}(-Q^2, 0, 0)/e^2$  coupling function used in the FIT 1 (2.22). The azure dash-dot-dotted line and the magenta long-dashed line are for  $b_{1\gamma^*\gamma^*}(-Q^2, 0, 0)/e^2$  and  $b_{0\gamma^*\gamma^*}(-Q^2, 0, 0)/e^2$ , respectively, in the FIT 2 (2.23). The  $a$  and  $b$  parameters are plotted in units  $\text{GeV}^{-3}$  and  $\text{GeV}^{-1}$ , respectively.

We assume, furthermore, that the  $t$  dependence of the  $\gamma^{(*)}p \rightarrow \gamma p$  amplitudes is described by the Regge factors and the following combined functions

$$F_{\text{eff}}^{(j)}(t) = F^{(j)}(t) \times F_1^{(j)}(t) = \exp(-b_j|t|/2). \quad (2.24)$$

Note that the same  $t$  dependence is assumed for both  $a$  and  $b$  coupling functions for a given  $j$  ( $j = 0, 1, 2$ ) in Eqs. (2.21)–(2.23). For our study here we assume  $b_1 = b_2$ . We take, for both FIT 1 and FIT 2 the same parameters,  $b_1 = b_2 = 5.0 \text{ GeV}^{-2}$  and  $b_0 = 1.0 \text{ GeV}^{-2}$  found by comparison of the theoretical curves to the experimental data for  $d\sigma/dt$ .

With this we have specified our model and given the parameter values for our two fits which we shall compare to the data in Sec. III.



### III. RESULTS

In this section we compare the tensor-pomeron model to the FNAL data [73] on real-photon-proton scattering ( $\gamma p \rightarrow \gamma p$ ), and to HERA data [17–20] on DVCS ( $\gamma^*(Q^2)p \rightarrow \gamma p$ ) for different averaged  $W$  and  $Q^2$ . We shall restrict our discussion to experimental results that satisfy the conditions  $x \approx Q^2/W^2 < 0.02$  and  $|t| \lesssim 1 \text{ GeV}^2$  where our model should be reliable. We also have to make a comment on *what* quantity is measured in [17]. For this we compare Eqs. (6)–(8) of [17] with Eqs. (2.5)–(2.7). We cannot see that longitudinally polarized  $\gamma^*$ 's do not contribute after integration over azimuthal angles, as is claimed in footnote 7 of [17]. Thus, to the best of our understanding, the cross section measured in [17] must be

$$\frac{d\sigma}{dt} = \frac{d\sigma_T}{dt} + \varepsilon \frac{d\sigma_L}{dt}, \quad (3.1)$$

where  $\varepsilon \approx 1$  for the HERA kinematic region. In the following we suppose that this is the case. We shall use the notation

$$\sigma(Q^2, W^2) = \int dt \frac{d\sigma}{dt}(Q^2, W^2, t) \quad (3.2)$$

and similarly for the T and L components.

In Fig. 3 we show the  $\gamma^{(*)}p \rightarrow \gamma p$  total cross sections as a function of the c.m. energy  $W$ . In the top panels we compare our fits, FIT 1 (left panel) and FIT 2 (right panel), to the FNAL result from [73]<sup>1</sup> where  $Q^2 = 0$  and to the HERA data from [17–20] for different values of  $Q^2$  (the average values). The complete cross section is a coherent sum of soft and hard components in the amplitude. These components have different energy dependence. For real Compton scattering ( $Q^2 = 0$ ) the cross section is dominated by soft-pomeron exchange with an additional contribution from reggeon exchange at lower energies. The hard-pomeron contribution is negligibly small there. The cross sections rise with energy as  $W^{2\epsilon_1}$  at  $Q^2 = 0$  and change to  $W^{2\epsilon_0}$  for very high  $Q^2$ . Here  $\epsilon_1 \approx 0.09$  and  $\epsilon_0 \approx 0.30$  are the intercept parameters of the soft and hard pomerons, respectively, see (2.14), (2.15). In our model the dominant contribution comes from the  $b$ -type coupling functions  $b_{j\gamma^*\gamma^*}$  ( $j = 0, 1$ ). Their size, as shown in Fig. 2, differs in the two fits. We see from the bottom panels of Fig. 3 that for higher  $Q^2$  the soft component slowly decreases relative to the hard one. A significant constructive interference effect between the soft and hard components is clearly visible. Here and in the following, the interference term is calculated as the difference of coherent and incoherent cross sections of the  $\mathbb{P}_1$ ,  $\mathbb{P}_0$ , and  $\mathbb{R}$  contributions. The Fits 1 and 2 hardly differ for the  $W$  region where there are data. But for higher  $W$  values FIT 2, where the contribution from the hard pomeron is enhanced, gives a steeper rise of the cross section with  $W$  and especially so for larger  $Q^2$ . Only future experiments will tell us what happens in nature.

In Fig. 4 we show how the cross section depends on  $Q^2$  for two c.m. energies  $W = 82$  and  $104 \text{ GeV}$ . Complete results for our two fits and the soft and hard components separately are shown together with the HERA data. From the top panels (for FIT 1) we see that the soft pomeron survives to relatively large  $Q^2$  and at  $Q^2 \simeq 50 \text{ GeV}^2$  the interference term plays an important role in the description of the data. From the bottom

---

<sup>1</sup> Note that in [73] the value of  $\sigma = 88 \pm 4 \text{ nb}$  for the elastic  $\gamma p$  cross section was given. This value was obtained by summing the beam-energy-averaged differential cross sections measured at c.m. energies  $W = 9.73 - 15.645 \text{ GeV}$  for  $|t| \geq 0.07 \text{ GeV}^2$  with those from the preferred fit II of [73] for  $|t| < 0.07 \text{ GeV}^2$ .

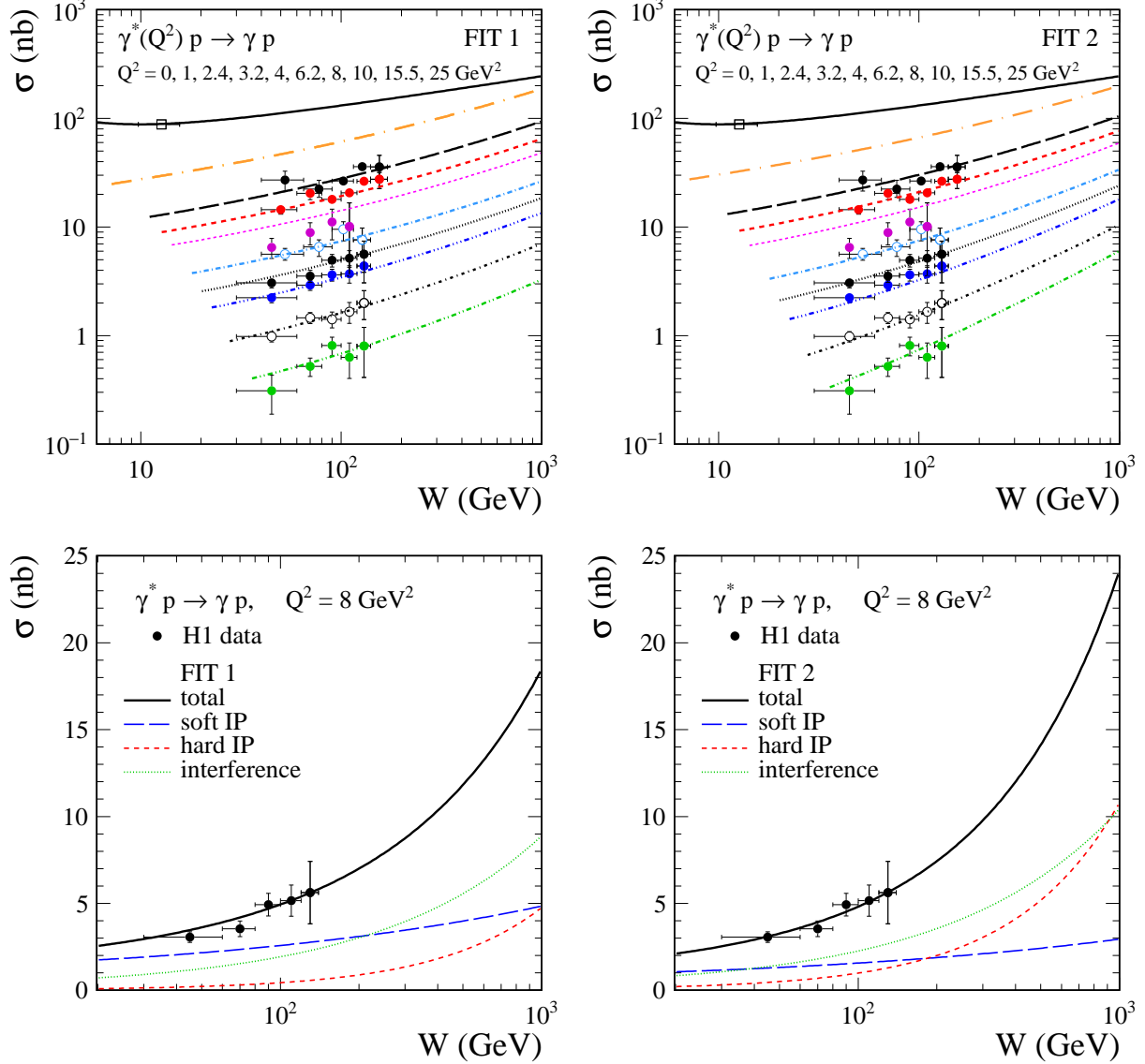


FIG. 3. Top panels: Total cross sections as a function of the c.m. energy  $W$  for FIT 1 (left) and FIT 2 (right). Comparison of theoretical results to the FNAL data from [73] for real Compton scattering ( $Q^2 = 0$ ) and to the DVCS HERA data is shown. The upper black solid line is for  $Q^2 = 0$ , the orange long-dashed-dotted line is for  $Q^2 = 1 \text{ GeV}^2$ . The remaining lines correspond to the values  $Q^2 = 2.4, 3.2, 4, 6.2, 8, 10, 15.5, 25 \text{ GeV}^2$  (from top to bottom) and should be compared with the HERA data from [17–20]. Bottom panels: Our fit results for  $Q^2 = 8 \text{ GeV}^2$  together with the H1 data [18]. We show the contributions for soft and hard pomeron separately, see the blue long-dashed line and the red dashed line, and their coherent sum (total), see the black solid line. The interference term is shown separately by the green dotted line.

panels (for FIT 2) one can observe that at  $Q^2 \simeq 50 \text{ GeV}^2$  the hard pomeron alone is able to describe the data. Here the contribution from the interference term is considerable for intermediate values of  $Q^2 \sim 10 \text{ GeV}^2$ . It is interesting to note that the interference effect is also large when the hard component reaches a maximum. For our fits this is at

$$Q^2 \cong 1.3 \text{ GeV}^2.$$

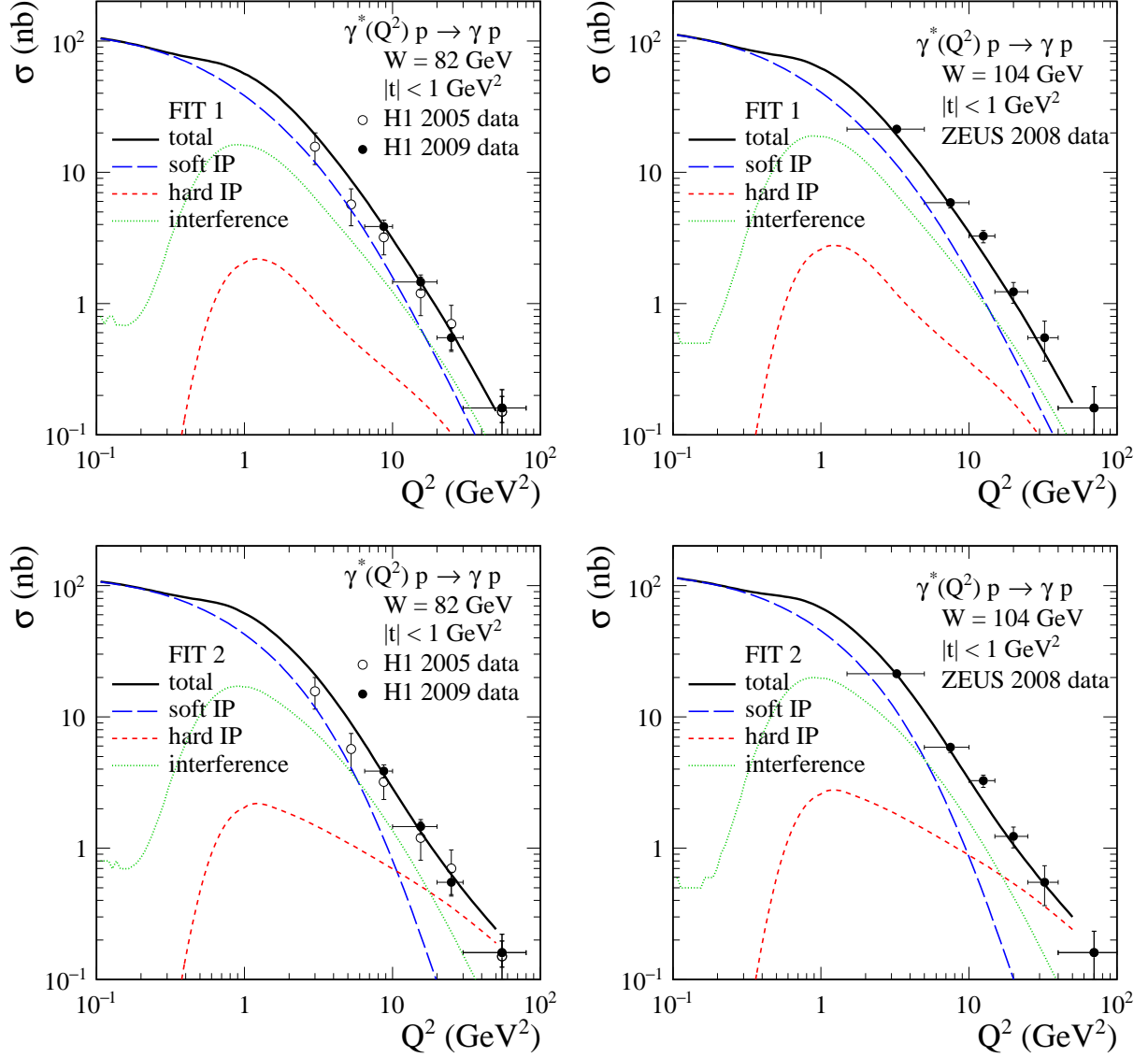


FIG. 4. Comparison of the cross sections for the  $\gamma^{(*)}(Q^2)p \rightarrow \gamma p$  reaction as a function of  $Q^2$  to the experimental data for  $\langle W \rangle = 82$  GeV from [17, 18] (left panels) and for  $\langle W \rangle = 104$  GeV from [20] (right panels). Results on top panels correspond to FIT 1 and those on the bottom panels to FIT 2. The meaning of the lines is the same as in the bottom panels of Fig. 3.

In Fig. 5 we show the differential cross sections  $d\sigma/dt$  from (3.1) with  $\varepsilon = 1$  for different  $\langle W \rangle$  and  $\langle Q^2 \rangle$ . In the top panels, the upper line corresponds to  $W = 12.7$  GeV and  $Q^2 = 0$  and should be compared to the averaged FNAL data (top data points) for the  $\gamma p \rightarrow \gamma p$  reaction [73]. In this kinematic range, for  $Q^2 = 0$  and at intermediate  $W$ , the reggeon plus soft-IP contributions dominate and the hard-IP exchange gives negligible contribution. As expected, there is a significant interference between the reggeon and soft-pomeron components. The slope parameters  $b_2$  and  $b_1$  in (2.24) are adjusted to the FNAL  $d\sigma/dt$  data on the real-photon-proton scattering. At higher  $W$  and  $Q^2$  measured at HERA the

hard pomeron plays an increasingly important role. The slope parameter  $b_0$  for the hard-pomeron exchange is adjusted to the DVCS HERA data. As we noted above,  $d\sigma(\gamma^*p \rightarrow \gamma p)/dt$  is the sum of two contributions  $d\sigma_T/dt$  and  $d\sigma_L/dt$  with the latter term becoming very small for  $|t| \rightarrow 0$ . This is understandable since for  $\gamma^*p \rightarrow \gamma p$  forward scattering only double-helicity-flip amplitudes can contribute to  $d\sigma_L/dt$ . Furthermore,  $d\sigma_T/dt$  is dominated by the  $b$ -type couplings and  $d\sigma_L/dt$  is dominated by the  $a$ -type couplings; see Eq. (2.17).

In Fig. 6 we show the complete theoretical result and individual components contributing to the cross section  $d\sigma/dt$ , see (3.1), for  $W = 82$  GeV and  $Q^2 = 8$  GeV<sup>2</sup> together with the H1 data [18]. The constructive interference of the soft and hard pomeron terms is again a salient feature.

We note that our complete result for  $d\sigma/dt$  does not have a simple exponential  $t$  dependence as is frequently assumed in other models. This is caused by the interference of soft- and hard-pomeron terms (each with different  $t$  dependence) and by the longitudinal contribution which is important for large  $|t|$ .

Figure 7 shows the ratios of the  $\gamma^*p \rightarrow \gamma p$  cross sections for longitudinally and transversely polarized virtual photons,

$$R(Q^2, W^2) = \frac{\sigma_L(Q^2, W^2)}{\sigma_T(Q^2, W^2)}, \quad (3.3)$$

$$\tilde{R}(Q^2, W^2, t) = \frac{\frac{d\sigma_L}{dt}(Q^2, W^2, t)}{\frac{d\sigma_T}{dt}(Q^2, W^2, t)}, \quad (3.4)$$

as functions of  $Q^2$  and  $|t|$ , respectively. The cross section  $\sigma_L$  vanishes proportionally to  $Q^2$  for  $Q^2 \rightarrow 0$ . The ratio  $\tilde{R}(Q^2, W^2, t)$  strongly grows with  $|t|$ . We must emphasize that this behaviour of  $\tilde{R}(Q^2, W^2, t)$  depends crucially on our (reasonable) assumption that  $a$  and  $b$  couplings in the  $\mathbb{P}\gamma^*\gamma^*$  vertex functions have the same  $t$  dependence for a given  $j$  ( $j = 0, 1, 2$ ); see (2.18), (2.19), and (2.24). But it is clear from the right panel of Fig. 7 that a very small ratio  $\tilde{R}(Q^2, W^2, t)$  for all  $|t| \lesssim 1.0$  GeV<sup>2</sup> could, in our model, only be achieved if the  $a$  and  $b$  couplings would have drastically different  $t$  dependences.

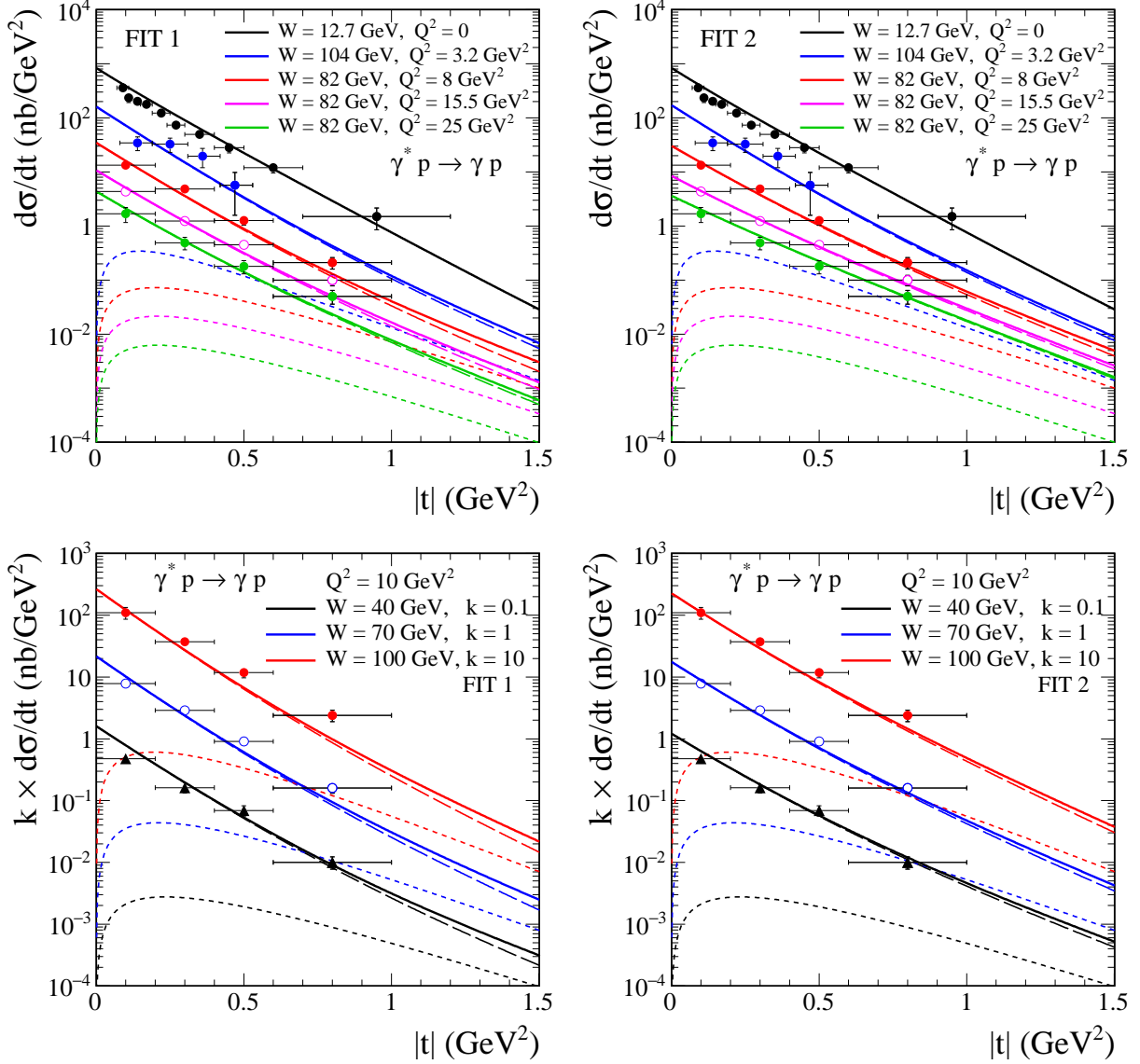


FIG. 5. Top panels: The differential cross sections  $d\sigma/dt$  compared to experimental data for different  $\gamma^* p$  c.m. energy and photon virtuality. The upper line corresponds to  $W = 12.7$  GeV and  $Q^2 = 0$  and averaged FNAL data [73]. The theoretical results for  $\gamma^* p \rightarrow \gamma p$  at higher  $W$  and  $Q^2$  for transverse (long-dashed lines) and longitudinal (short-dashed lines) polarization of the  $\gamma^*$  and their sum (solid lines) are shown together with experimental data. Data for  $\langle W \rangle = 104$  GeV are from [20] and for  $\langle W \rangle = 82$  GeV from [18]. Bottom panels: Comparison of the fit results to the H1 data [18] for  $\langle Q^2 \rangle = 10$  GeV<sup>2</sup> and  $\langle W \rangle = 40, 70$ , and  $100$  GeV (from bottom to top). Here we show the results scaled by a factor  $k$  (specified in the figure legend) for displaying purposes.

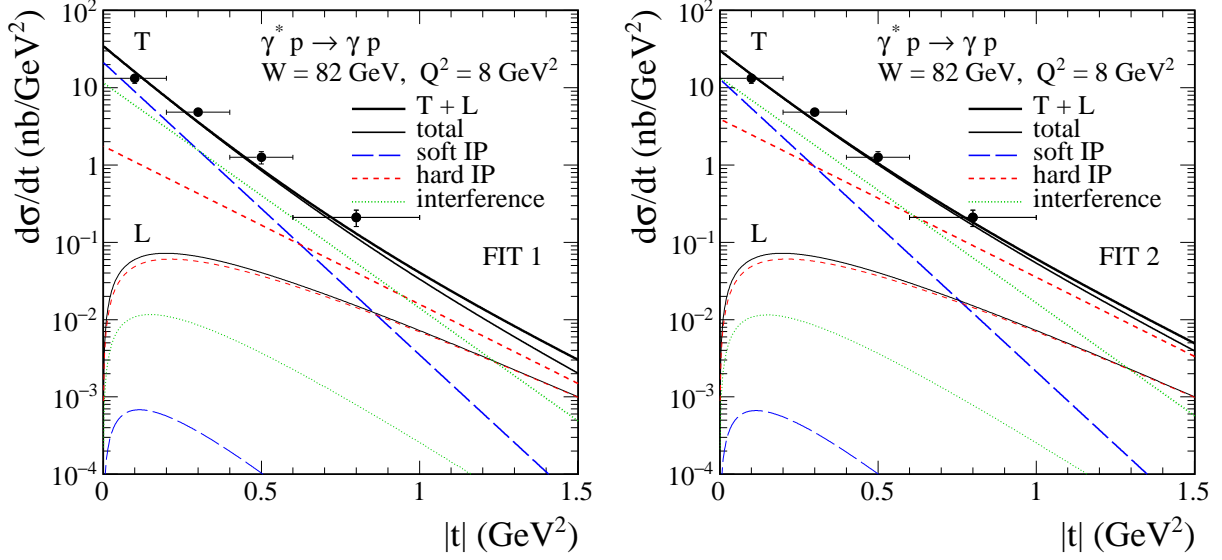


FIG. 6. Comparison of the FIT 1 (left) and the FIT 2 (right) to DVCS H1 data [18] for  $W = 82$  GeV and  $Q^2 = 8$  GeV<sup>2</sup>. The results for  $\gamma^* p \rightarrow \gamma p$  for transverse (T) and longitudinal (L) polarization of the  $\gamma^*$  individually and their sum T + L (see the upper solid lines) are shown. The contributions of soft IP (the blue short-dashed lines), hard IP (the red long-dashed lines), the interference term (the green dotted lines), and their sum total (the thin full lines) for T and L components individually are also shown.

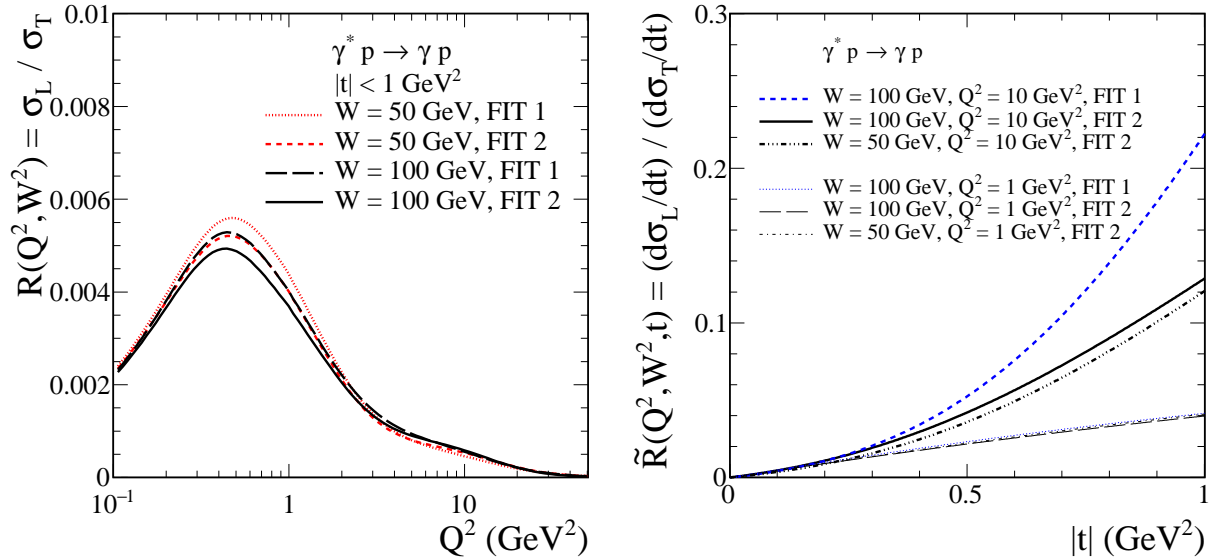


FIG. 7. The ratios of cross sections  $R(Q^2, W^2)$  (3.3) and  $\tilde{R}(Q^2, W^2, t)$  (3.4) for the  $\gamma^* p \rightarrow \gamma p$  reaction for longitudinally and transversely polarized  $\gamma^*$ . Note that the meaning of the lines on these two panels is different.

#### IV. CONCLUSIONS AND DISCUSSION

In the present paper we have applied the tensor-pomeron approach to deeply virtual Compton scattering (DVCS) for high c.m. energies  $W$  and small Bjorken- $x$ ,  $x \lesssim 0.02$ .

We have made a comparison of the two-tensor-pomeron model to the DVCS data measured at HERA. As a starting point we have used the fit parameters of the intercepts of the two pomerons and of the reggeon  $\mathbb{R}_+$ , and their coupling functions to real and virtual photons determined in [1] from deep inelastic scattering (DIS) and real photoabsorption cross sections. To our surprise, with a ‘minimal’, but reasonable, modification of the  $Q^2$  dependence of only one  $\gamma^*(Q^2)\gamma\mathbb{P}$  coupling function [FIT 1 (2.22)] we have already got a good fit to the experimental data. We could describe the  $W$ ,  $Q^2$  and  $t$  dependences of  $d\sigma(\gamma^*p \rightarrow \gamma p)/dt$  measured at HERA and of the elastic photon-proton cross section measured at FNAL. The good description of the DVCS data is achieved due to a sizeable interference of soft and hard pomeron contributions. We have considered also FIT 2 (2.23) in which the size of the hard-pomeron component was increased, especially for larger  $Q^2$ , and the soft-pomeron component was reduced relative to FIT 1. We kept here, on purpose, the same parameters of the form factors (2.24) as in FIT 1. The FIT 2 better describes the data at larger  $|t|$  for  $Q^2 \gtrsim 8 \text{ GeV}^2$  (see Fig. 5). Note that in our two-tensor-pomeron model the soft component and also the interference of soft and hard terms are very important up to at least  $Q^2 \simeq 20 \text{ GeV}^2$ .

We consider it as a very satisfactory feature of our approach for DVCS that we describe in the same framework both the low  $Q^2$  and high  $Q^2$  regimes and the transition between them. The same situation was shown to be true for DIS in [1]. Going from reactions with virtual or real photons ( $Q^2 \leq 0$ ) to hadronic reactions is straightforward in the tensor-pomeron model. Indeed, in the original paper on the tensor-pomeron model [46] hadronic reactions were the main focus, but already there photon-induced reactions were considered and general remarks on the vector-meson-dominance (VMD) model were made. It can be seen from Refs. [1, 46–56] and the present paper that the tensor-pomeron model is applicable to soft high-energy reactions which are purely hadronic as well as to reactions involving photons and hadrons.

Now we comment on Refs. [44, 45] where also Regge theory is applied to DVCS. These authors consider, as far as we can see, only leading helicity amplitudes. For DVCS this means that only transversely polarized initial  $\gamma^*$ ’s are considered. In contrast, in our tensor-pomeron approach we present a complete model, including *all* helicity amplitudes. Therefore, we could make, e.g., predictions for  $\sigma_L/\sigma_T$  which can and should be checked by experiments. Also, our model for DVCS gives different relations between soft and hard terms compared to the analysis of [45], see Sec. IV therein, and also the reviews [71, 74] where more results are presented. The contribution from the interference term found in [45] is considerable for intermediate values of  $Q^2$ , but smaller than our findings (FIT 1 and FIT 2).

In our calculations we have included the contributions of both transverse and longitudinal virtual photons. The longitudinal cross section  $d\sigma_L(Q^2, W^2, t)/dt$  is predicted to be very small for  $|t| \rightarrow 0$  but to be sizeable for  $0.5 \text{ GeV}^2 \lesssim |t| \lesssim 1.0 \text{ GeV}^2$  (see Figs. 5 and 6). The corresponding ratio of L/T grows strongly with  $|t|$  (see the right panel of Fig. 7). We have also shown the  $Q^2$  dependence of this ratio for different c.m. energies of the  $\gamma^*p$  system.

To summarize, we have presented predictions for low- $x$  DVCS of the two-tensor-

pomeron model which previously was successfully applied to low  $x$  DIS in [1]. The model provides amplitudes for all helicity configurations and, thus, can be checked by experimentalists in many ways. We are looking forward to further tests of the non-perturbative QCD dynamics embodied in our tensor-pomeron exchanges in future electron-hadron collisions in the low- $x$  regime at the EIC and LHeC colliders.

## ACKNOWLEDGMENTS

The authors are grateful to Markus Diehl for correspondence and comments and to Carlo Ewerz for useful discussions. This work was partially supported by the Polish National Science Centre Grant No. 2018/31/B/ST2/03537. P. L. was supported by the Bekker Program of the Polish National Agency for Academic Exchange, Project No. BPN/BEK/2021/2/00009/U/00001.

- 
- [1] D. Britzger, C. Ewerz, S. Glazov, O. Nachtmann, and S. Schmitt, *Tensor Pomeron and low- $x$  deep inelastic scattering*, Phys. Rev. **D100** no. 11, (2019) 114007, arXiv:1901.08524 [hep-ph].
  - [2] X.-D. Ji, *Deeply virtual Compton scattering*, Phys. Rev. D **55** (1997) 7114, arXiv:hep-ph/9609381.
  - [3] M. Diehl, T. Gousset, B. Pire, and J. P. Ralston, *Testing the handbag contribution to exclusive virtual Compton scattering*, Phys. Lett. B **411** (1997) 193, arXiv:hep-ph/9706344.
  - [4] J. Bartels and M. Loewe, *The Nonforward QCD Ladder Diagrams*, Z. Phys. C **12** (1982) 263.
  - [5] M. Diehl, *Generalized parton distributions*, Phys. Rept. **388** (2003) 41, arXiv:hep-ph/0307382.
  - [6] M. Diehl and S. Sapeta, *On the analysis of lepton scattering on longitudinally or transversely polarized protons*, Eur. Phys. J. C **41** (2005) 515, arXiv:hep-ph/0503023.
  - [7] M. V. T. Machado, *Nuclear DVCS at small  $x$  using the color-dipole phenomenology*, Eur. Phys. J. C **59** (2009) 769, arXiv:0810.3665 [hep-ph].
  - [8] B. Z. Kopeliovich, I. Schmidt, and M. Siddikov, *Deeply virtual Compton scattering via color dipoles: Nonperturbative effects*, Phys. Rev. D **79** (2009) 034019, arXiv:0812.3992 [hep-ph].
  - [9] V. M. Braun, A. N. Manashov, D. Müller, and B. M. Pirnay, *Deeply Virtual Compton Scattering to the twist-four accuracy: Impact of finite- $t$  and target mass corrections*, Phys. Rev. D **89** no. 7, (2014) 074022, arXiv:1401.7621 [hep-ph].
  - [10] B. Kriesten, S. Liuti, L. Calero-Diaz, D. Keller, A. Meyer, G. R. Goldstein, and J. Osvaldo Gonzalez-Hernandez, *Extraction of generalized parton distribution observables from deeply virtual electron proton scattering experiments*, Phys. Rev. D **101** no. 5, (2020) 054021, arXiv:1903.05742 [hep-ph].
  - [11] H. Dutrieux, C. Lorcé, H. Moutarde, P. Sznajder, A. Trawiński, and J. Wagner, *Phenomenological assessment of proton mechanical properties from deeply virtual Compton scattering*, Eur. Phys. J. C **81** no. 4, (2021) 300, arXiv:2101.03855 [hep-ph].
  - [12] D. Bendova, J. Cepila, V. P. Gonçalves, and C. R. Sena, *Deeply virtual Compton scattering at the EIC and LHeC: a comparison among saturation approaches*, Eur. Phys. J. C **82** no. 2, (2022) 99.
  - [13] Y.-P. Xie and V. P. Goncalves, *Exclusive processes in  $ep$  collisions at the EIC and LHeC: A closer look on the predictions of saturation models*, Phys. Rev. D **105** no. 1, (2022) 014033, arXiv:2201.10499 [hep-ph].



- [14] V. P. Gonçalves, D. E. Martins, and C. R. Sena, *Coherent and incoherent deeply virtual Compton scattering in electron–ion collisions at the EIC and LHeC*, Eur. Phys. J. A **58** no. 2, (2022) 18.
- [15] N. d’Hose, S. Niccolai, and A. Rostomyan, *Experimental overview of Deeply Virtual Compton Scattering*, Eur. Phys. J. A **52** no. 6, (2016) 151.
- [16] E.-C. Aschenauer, S. Fazio, K. Kumericki, and D. Mueller, *Deeply virtual Compton Scattering at a proposed high-luminosity Electron-Ion Collider*, JHEP **09** (2013) 093, arXiv:1304.0077 [hep-ph].
- [17] A. Aktas *et al.*, (H1 Collaboration), *Measurement of deeply virtual Compton scattering at HERA*, Eur. Phys. J. C **44** (2005) 1, arXiv:hep-ex/0505061.
- [18] F. D. Aaron *et al.*, (H1 Collaboration), *Deeply virtual Compton scattering and its beam charge asymmetry in  $e^\pm p$  collisions at HERA*, Phys. Lett. B **681** (2009) 391, arXiv:0907.5289 [hep-ex].
- [19] S. Chekanov *et al.*, (ZEUS Collaboration), *Measurement of deeply virtual Compton scattering at HERA*, Phys. Lett. B **573** (2003) 46, arXiv:hep-ex/0305028.
- [20] S. Chekanov *et al.*, (ZEUS Collaboration), *A measurement of the  $Q^2$ ,  $W$  and  $t$  dependences of deeply virtual Compton scattering at HERA*, JHEP **05** (2009) 108, arXiv:0812.2517 [hep-ex].
- [21] A. Airapetian *et al.*, (HERMES), *Measurement of double-spin asymmetries associated with deeply virtual Compton scattering on a transversely polarized hydrogen target*, Phys. Lett. B **704** (2011) 15, arXiv:1106.2990 [hep-ex].
- [22] A. Airapetian *et al.*, (HERMES Collaboration), *Beam-helicity and beam-charge asymmetries associated with deeply virtual Compton scattering on the unpolarised proton*, JHEP **07** (2012) 032, arXiv:1203.6287 [hep-ex].
- [23] A. Airapetian *et al.*, (HERMES Collaboration), *Beam-helicity asymmetry arising from deeply virtual Compton scattering measured with kinematically complete event reconstruction*, JHEP **10** (2012) 042, arXiv:1206.5683 [hep-ex].
- [24] F. X. Girod *et al.*, (CLAS Collaboration), *Measurement of Deeply virtual Compton Scattering Beam-Spin Asymmetries*, Phys. Rev. Lett. **100** (2008) 162002, arXiv:0711.4805 [hep-ex].
- [25] H. S. Jo *et al.*, (CLAS Collaboration), *Cross Sections for the Exclusive Photon Electroproduction on the Proton and Generalized Parton Distributions*, Phys. Rev. Lett. **115** no. 21, (2015) 212003, arXiv:1504.02009 [hep-ex].
- [26] N. Hirlinger Saylor *et al.*, (CLAS), *Measurement of Unpolarized and Polarized Cross Sections for Deeply Virtual Compton Scattering on the Proton at Jefferson Laboratory with CLAS*, Phys. Rev. C **98** no. 4, (2018) 045203, arXiv:1810.02110 [hep-ex].
- [27] V. Burkert *et al.*, (CLAS Collaboration), *Beam charge asymmetries for deeply virtual Compton scattering off the proton*, Eur. Phys. J. A **57** no. 6, (2021) 186, arXiv:2103.12651 [nucl-ex].
- [28] S. Chen *et al.*, (CLAS), *Measurement of Deeply Virtual Compton Scattering with a Polarized Proton Target*, Phys. Rev. Lett. **97** (2006) 072002, arXiv:hep-ex/0605012.
- [29] E. Seder *et al.*, (CLAS Collaboration), *Longitudinal Target-Spin Asymmetries for Deeply Virtual Compton Scattering*, Phys. Rev. Lett. **114** no. 3, (2015) 032001, arXiv:1410.6615 [hep-ex]. [Erratum: Phys.Rev.Lett. 114, 089901 (2015)].
- [30] S. Pisano *et al.*, (CLAS Collaboration), *Single and double spin asymmetries for deeply virtual Compton scattering measured with CLAS and a longitudinally polarized proton target*, Phys. Rev. D **91** no. 5, (2015) 052014, arXiv:1501.07052 [hep-ex].
- [31] R. Akhunzyanov *et al.*, (COMPASS Collaboration), *Transverse extension of partons in the proton probed in the sea-quark range by measuring the DVCS cross section*, Phys. Lett. B **793** (2019) 188, arXiv:1802.02739 [hep-ex]. [Erratum: Phys.Lett.B 800, 135129 (2020)].
- [32] C. Muñoz Camacho *et al.*, (Jefferson Lab Hall A Collaboration), *Scaling Tests of the Cross Section for Deeply Virtual Compton Scattering*, Phys. Rev. Lett. **97** (2006) 262002,

arXiv:nucl-ex/0607029.

- [33] M. Defurne *et al.*, (Jefferson Lab Hall A), *E00-110 experiment at Jefferson Lab Hall A: Deeply virtual Compton scattering off the proton at 6 GeV*, Phys. Rev. C **92** no. 5, (2015) 055202, arXiv:1504.05453 [nucl-ex].
- [34] M. Mazouz *et al.*, (Jefferson Lab Hall A), *Deeply Virtual Compton Scattering off the Neutron*, Phys. Rev. Lett. **99** (2007) 242501, arXiv:0709.0450 [nucl-ex].
- [35] F. Georges *et al.*, (Jefferson Lab Hall A Collaboration), *Deeply Virtual Compton Scattering Cross Section at High Bjorken  $x_B$* , Phys. Rev. Lett. **128** no. 25, (2022) 252002, arXiv:2201.03714 [hep-ph].
- [36] A. Accardi *et al.*, *Electron-Ion Collider: The Next QCD Frontier: Understanding the glue that binds us all*, Eur. Phys. J. A **52** no. 9, (2016) 268, arXiv:1212.1701 [nucl-ex].
- [37] E. C. Aschenauer, S. Fazio, J. H. Lee, H. Mantysaari, B. S. Page, B. Schenke, T. Ullrich, R. Venugopalan, and P. Zurita, *The electron-ion collider: assessing the energy dependence of key measurements*, Rept. Prog. Phys. **82** no. 2, (2019) 024301, arXiv:1708.01527 [nucl-ex].
- [38] R. Abdul Khalek *et al.*, *Science Requirements and Detector Concepts for the Electron-Ion Collider: EIC Yellow Report*, Nucl. Phys. A **1026** (2022) 122447, arXiv:2103.05419 [physics.ins-det].
- [39] J. L. Abelleira Fernandez *et al.*, (LHeC Study Group), *A Large Hadron Electron Collider at CERN: Report on the Physics and Design Concepts for Machine and Detector*, J. Phys. G **39** (2012) 075001, arXiv:1206.2913 [physics.acc-ph].
- [40] P. Agostini *et al.*, (LHeC, FCC-he Study Group), *The Large Hadron-Electron Collider at the HL-LHC*, J. Phys. G **48** no. 11, (2021) 110501, arXiv:2007.14491 [hep-ex].
- [41] P. D. B. Collins, *An Introduction to Regge Theory and High-Energy Physics*. Cambridge University Press, Cambridge, England, 1977.
- [42] L. Caneschi, ed., *Regge Theory of Low- $p_t$  Hadronic Interactions*. Elsevier Science Publishers B.V., Amsterdam, 1989.
- [43] A. Donnachie, H. G. Dosch, P. V. Landshoff, and O. Nachtmann, *Pomeron physics and QCD*, Camb.Monogr.Part.Phys.Nucl.Phys.Cosmol. **19** (2002) 1.
- [44] M. Capua, S. Fazio, R. Fiore, L. L. Jenkovszky, and F. Paccanoni, *A deeply virtual Compton scattering amplitude*, Phys. Lett. B **645** (2007) 161, arXiv:hep-ph/0605319.
- [45] S. Fazio, R. Fiore, L. Jenkovszky, and A. Salii, *Unifying “soft” and “hard” diffractive exclusive vector meson production and deeply virtual Compton scattering*, Phys. Rev. D **90** no. 1, (2014) 016007, arXiv:1312.5683 [hep-ph].
- [46] C. Ewerz, M. Maniatis, and O. Nachtmann, *A Model for Soft High-Energy Scattering: Tensor Pomeron and Vector Odderon*, Annals Phys. **342** (2014) 31, arXiv:1309.3478 [hep-ph].
- [47] A. Bolz, C. Ewerz, M. Maniatis, O. Nachtmann, M. Sauter, and A. Schöning, *Photoproduction of  $\pi^+\pi^-$  pairs in a model with tensor-pomeron and vector-odderon exchange*, JHEP **1501** (2015) 151, arXiv:1409.8483 [hep-ph].
- [48] P. Lebiedowicz, O. Nachtmann, and A. Szczurek, *Exclusive central diffractive production of scalar and pseudoscalar mesons; tensorial vs. vectorial pomeron*, Annals Phys. **344** (2014) 301, arXiv:1309.3913 [hep-ph].
- [49] P. Lebiedowicz, O. Nachtmann, and A. Szczurek,  *$\rho^0$  and Drell-Söding contributions to central exclusive production of  $\pi^+\pi^-$  pairs in proton-proton collisions at high energies*, Phys. Rev. **D91** (2015) 074023, arXiv:1412.3677 [hep-ph].
- [50] P. Lebiedowicz, O. Nachtmann, and A. Szczurek, *Central exclusive diffractive production of the  $\pi^+\pi^-$  continuum, scalar, and tensor resonances in  $pp$  and  $p\bar{p}$  scattering within the tensor Pomeron approach*, Phys. Rev. **D93** (2016) 054015, arXiv:1601.04537 [hep-ph].

- [51] P. Lebiedowicz, O. Nachtmann, and A. Szczurek, *Searching for the odderon in  $pp \rightarrow ppK^+K^-$  and  $pp \rightarrow pp\mu^+\mu^-$  reactions in the  $\phi(1020)$  resonance region at the LHC*, Phys. Rev. D **101** (2020) 094012, arXiv:1911.01909 [hep-ph].
- [52] P. Lebiedowicz, O. Nachtmann, and A. Szczurek, *Central exclusive diffractive production of  $K^+K^-K^+K^-$  via the intermediate  $\phi\phi$  state in proton-proton collisions*, Phys. Rev. D **99** no. 9, (2019) 094034, arXiv:1901.11490 [hep-ph].
- [53] P. Lebiedowicz, J. Leutgeb, O. Nachtmann, A. Rebhan, and A. Szczurek, *Central exclusive diffractive production of axial-vector  $f_1(1285)$  and  $f_1(1420)$  mesons in proton-proton collisions*, Phys. Rev. D **102** no. 11, (2020) 114003, arXiv:2008.07452 [hep-ph].
- [54] P. Lebiedowicz, O. Nachtmann, and A. Szczurek, *High-energy  $\pi\pi$  scattering without and with photon radiation*, Phys. Rev. D **105** no. 1, (2022) 014022, arXiv:2107.10829 [hep-ph].
- [55] P. Lebiedowicz, O. Nachtmann, and A. Szczurek, *Soft-photon radiation in high-energy proton-proton collisions within the tensor-Pomeron approach: Bremsstrahlung*, Phys. Rev. D **106** no. 3, (2022) 034023, arXiv:2206.03411 [hep-ph].
- [56] C. Ewerz, P. Lebiedowicz, O. Nachtmann, and A. Szczurek, *Helicity in Proton-Proton Elastic Scattering and the Spin Structure of the Pomeron*, Phys. Lett. B **763** (2016) 382, arXiv:1606.08067 [hep-ph].
- [57] L. Adamczyk *et al.*, (STAR Collaboration), *Single spin asymmetry  $A_N$  in polarized proton-proton elastic scattering at  $\sqrt{s} = 200$  GeV*, Phys. Lett. B **719** (2013) 62, arXiv:1206.1928 [nucl-ex].
- [58] S. K. Domokos, J. A. Harvey, and N. Mann, *Pomeron contribution to  $pp$  and  $p\bar{p}$  scattering in AdS/QCD*, Phys. Rev. D **80** (2009) 126015, arXiv:0907.1084 [hep-ph].
- [59] I. Iatrakis, A. Ramamurti, and E. Shuryak, *Pomeron Interactions from the Einstein-Hilbert Action*, Phys. Rev. D **94** no. 4, (2016) 045005, arXiv:1602.05014 [hep-ph].
- [60] A. Donnachie and P. V. Landshoff, *Small  $x$ : two pomerons!*, Phys. Lett. B **437** (1998) 408, arXiv:hep-ph/9806344.
- [61] H. Abramowicz *et al.*, (H1 and ZEUS Collaborations), *Combination of measurements of inclusive deep inelastic  $e^\pm p$  scattering cross sections and QCD analysis of HERA data*, Eur. Phys. J. C **75** no. 12, (2015) 580, arXiv:1506.06042 [hep-ex].
- [62] T. Arens, O. Nachtmann, M. Diehl, and P. V. Landshoff, *Some tests for the helicity structure of the pomeron in  $ep$  collisions*, Z.Phys. C **74** (1997) 651, arXiv:hep-ph/9605376 [hep-ph].
- [63] L. N. Hand, *Experimental Investigation of Pion Electroproduction*, Phys. Rev. **129** (1963) 1834.
- [64] M. M. Brisudova, L. Burakovsky, and J. T. Goldman, *Effective functional form of Regge trajectories*, Phys. Rev. D **61** (2000) 054013, arXiv:hep-ph/9906293.
- [65] A. Tang and J. W. Norbury, *Properties of Regge trajectories*, Phys. Rev. D **62** (2000) 016006, arXiv:hep-ph/0004078.
- [66] R. Fiore, L. L. Jenkovszky, V. Magas, F. Paccanoni, and A. Papa, *Analytic model of Regge trajectories*, Eur. Phys. J. A **10** (2001) 217, arXiv:hep-ph/0011035.
- [67] H. Boschi-Filho, N. R. F. Braga, and H. L. Carrion, *Glueball Regge trajectories from gauge/string duality and the pomeron*, Phys. Rev. D **73** (2006) 047901, arXiv:hep-th/0507063.
- [68] A. A. Godizov and V. A. Petrov, *Nonlinearity of Regge trajectories in the scattering region*, JHEP **07** (2007) 083, arXiv:hep-ph/0701121.
- [69] R. Fiore, L. L. Jenkovszky, R. Orava, E. Predazzi, A. Prokudin, and O. Selyugin, *Forward Physics at the LHC: Elastic Scattering*, Int. J. Mod. Phys. A **24** (2009) 2551, arXiv:0810.2902 [hep-ph].
- [70] L. Jenkovszky, I. Szanyi, and C.-I. Tan, *Shape of proton and the pion cloud*, Eur. Phys. J. A **54** no. 7, (2018) 116, arXiv:1710.10594 [hep-ph].

- [71] L. Jenkovszky, R. Schicker, and I. Szanyi, *Elastic and diffractive scatterings in the LHC era*, Int. J. Mod. Phys. E **27** no. 08, (2018) 1830005, arXiv:1902.05614 [hep-ph].
- [72] I. Szanyi, L. Jenkovszky, R. Schicker, and V. Svintozelskyi, *Pomeron/glueball and odderon/oddball trajectories*, Nucl. Phys. A **998** (2020) 121728, arXiv:1910.02494 [hep-ph].
- [73] A. M. Breakstone, D. C. Cheng, D. E. Dorfan, A. A. Grillo, C. A. Heusch, V. Palladino, T. Schalk, A. Seiden, and D. B. Smith, *Elastic Photon-Proton Scattering in the 50-130 GeV Range*, Phys. Rev. Lett. **47** (1981) 1778.
- [74] L. Jenkovszky, *Spin and Polarization in High-Energy Hadron-Hadron and Lepton-Hadron Scattering*, Symmetry **12** no. 11, (2020) 1784, arXiv:2011.06432 [hep-ph].